

## A HIGH-QUALITY VELOCITY-DELAY MAP OF THE BROAD-LINE REGION IN NGC 5548

MING XIAO,<sup>1,2,3</sup> PU DU,<sup>2</sup> KAI-KING LU,<sup>1</sup> CHEN HU,<sup>2</sup> YAN-RONG LI,<sup>2</sup> ZHI-XIANG ZHANG,<sup>2</sup> KAI WANG,<sup>2</sup> YING-KE HUANG,<sup>2</sup>  
JIN-MING BAI,<sup>1</sup> WEI-HAO BIAN,<sup>4</sup> LUIS C. HO,<sup>5,6</sup> YE-FEI YUAN,<sup>7</sup> AND JIAN-MIN WANG<sup>2,3,8</sup>

<sup>1</sup>*Yunnan Observatory, Chinese Academy of Sciences, Kunming 650011, Yunnan, China*

<sup>2</sup>*Key Laboratory for Particle Astrophysics, Institute of High Energy Physics, Chinese Academy of Sciences, 19B Yuquan Road, Beijing 100049, China*

<sup>3</sup>*University of Chinese Academy of Sciences, 19A Yuquan Road, Beijing 100049, China*

<sup>4</sup>*Physics Department, Nanjing Normal University, Nanjing 210097, China*

<sup>5</sup>*Kavli Institute for Astronomy and Astrophysics, Peking University, Beijing 100871, China*

<sup>6</sup>*Department of Astronomy, School of Physics, Peking University, Beijing 100871, China*

<sup>7</sup>*Department of Astronomy, University of Science and Technology of China, Hefei 230026, China*

<sup>8</sup>*National Astronomical Observatories of China, Chinese Academy of Sciences, 20A Datun Road, Beijing 100020, China*

(Received 2018 August 3; Revised 2018 September 3; Accepted 2018 September 5)

### ABSTRACT

NGC 5548 has been well spectroscopically monitored for reverberation mapping of the central kinematics by 19 campaigns. Using the maximum entropy method in this Letter, we build up a high-quality velocity-delay map of the  $H\beta$  emission line in the light curves of the continuum and the line variations observed between 2015-2016. The map shows the response strength and lags of the velocity fields of the  $H\beta$  emitting regions. The velocity-delay structure of the map is generally symmetric, with strong red and blue wings at time lag  $\tau \lesssim 15$  days, a narrower velocity distribution at  $\tau \gtrsim 15$  days, and a deficit of response in the core. This is suggestive of a disk geometry of the broad-line region (BLR). The relatively weaker  $H\beta$  response at the longer lags in the red side indicates anisotropic emission from the outer part of the BLR. We also recover the velocity-delay maps of NGC 5548 from the historical data of 13 years to investigate the long-term variability of its BLR. In general, the BLR of NGC 5548 was switching between the inflow and virialized phases in the past years. The resultant maps of seven years reveal inflow signatures and show decreasing lags, indicating that the changes in the BLR size are related to the infalling BLR gas. The other four maps show potential disk signatures which are similar to our map.

*Keywords:* galaxies: active – galaxies: nuclei – galaxies: individual (NGC 5548) – galaxies: Seyfert

### 1. INTRODUCTION

Broad emission lines are the most prominent features of type 1 active galactic nuclei (AGNs). It is now generally accepted that these Doppler-broadened lines arise from the clouds in the broad-line region (BLR) photoionized by the central continuum radiation. Reverberation mapping (RM, see Bahcall et al. 1972; Blandford & McKee 1982; Peterson et al. 1993) has been widely used to investigate the geometry and kinematics of the BLRs in AGNs (Kaspi et al. 2000; Peterson et al. 2004; Denney et al. 2010; Bentz et al. 2010a; Grier et al. 2012; Du et al. 2018). The variations of the continuum ( $\Delta C$ ) and the emission line ( $\Delta L$ ) are connected as

the expression:

$$\Delta L(v, t) = \int_0^\infty \Psi(v, \tau) \Delta C(t - \tau) d\tau, \quad (1)$$

where  $\Psi(v, \tau)$  is the so-called “transfer function” or velocity-delay map. The map gives the distribution of the line response over the line-of-sight velocity  $v$  and the time delay  $\tau$ , and can be used to indicate the nature of the BLR.

Due to the limitation of data quality, early attempts mainly focus on analyzing the time lags as a function of the line-of-sight velocity (velocity-resolved time-lag analysis, see, e.g., Barth et al. 2011a,b; Bentz et al. 2008, 2009, 2010a; Denney et al. 2009a,b, 2010; Doroshenko et al. 2012; Du et al. 2016; Grier et al. 2013; Lu et al. 2016; Pei et al. 2017; De Rosa et al. 2015; Ulrich & Horne 1996). Velocity-resolved time-lag analysis has been applied to more than two dozen sources, and preliminarily reveals their BLR geometry and

kinematics. However, this method measures the mean time lags in each velocity bins rather than recover the velocity-delay maps which can reveal the detailed response features. Subsequently, more advanced techniques such as the maximum entropy method (MEM, Horne et al. 1991; Horne 1994; Xiao et al. 2018), regularized linear inversion method (RLI, Krolik & Done 1995; Skielboe et al. 2015) and the dynamical modeling method (Pancoast et al. 2011, 2014a; Li et al. 2013) begin to be applied to recover the velocity-delay maps (Bentz et al. 2010b; Grier et al. 2013, 2017; Pancoast et al. 2012, 2014b, 2018; Ulrich & Horne 1996; Xiao et al. 2018). Briefly speaking, MEM and RLI directly recover the velocity-delay map without adopting any specific model for the geometry and dynamics of the BLR. Dynamical modeling method fits the variations of the emission line profile by assuming specific BLR model, which can provide the velocity-delay map and the black hole mass measurement simultaneously.

As one of the most intensively observed objects in the RM study, NGC 5548 has been monitored by 19 individual campaigns, including the International AGN Watch Consortium (Peterson et al. 2002, and references therein), Bentz et al. (2007), Denney et al. (2009b), the 2008 Lick AGN Monitoring Project (LAMP2008; Bentz et al. 2009), the AGN Space Telescope and Optical Reverberation Mapping (AGN STORM; De Rosa et al. 2015; Edelson et al. 2015; Fausnaugh et al. 2016; Pei et al. 2017) and Lu et al. (2016). Three velocity-resolved time-lag analyses for the H $\beta$  line of NGC 5548 were presented, which reveal a velocity-symmetric line response and suggest that the BLR of NGC 5548 tends to be virialized or a Keplerian disk (Denney et al. 2009b; Lu et al. 2016; Pei et al. 2017). The velocity-resolved time-lag measurement of LAMP2008 data shows similar time lags in each velocity bins (Bentz et al. 2009), but the corresponding dynamical modeling analysis suggests that the dynamics of the BLR is dominated by inflow (Pancoast et al. 2014b). The velocity-delay map of LAMP2008 recovered by the RLI analysis is in general consistent with the velocity-resolved result, but shows a prompt response in the red wing (Skielboe et al. 2015). In addition, Kollatschny & Zetzl (2013) investigated the BLR geometry through the profiles of the emission lines of NGC 5548, and proposed that its BLR conforms to the disk wind model (Murray & Chiang 1997; Proga & Kallman 2004), and the geometry tends to be not thick.

In 2015, we started an RM campaign of NGC 5548 to investigate its BLR physics. The mean and velocity-resolved time lags have been presented in Lu et al. (2016). This Letter recovers the velocity-delay map of NGC 5548 by using MEM. In addition, to study the long-term variations of its BLR kinematics and geometry, we also analyze the AGN watch data of 13 years and recover the corresponding velocity-delay maps.

## 2. OBSERVATIONS AND DATA REDUCTION

The spectroscopic data used in this Letter were obtained in our RM campaign during 2015 January-July, by using the Yunnan Faint Object Spectrograph and Camera mounted in the 2.4 m telescope at Lijiang Station of Yunnan Observatories of Chinese Academy of Sciences. The details of the observation and data reduction were provided in Lu et al. (2016). For completeness, we briefly introduce some general points here. (1) We oriented the long slit (2".5 wide) to take the spectra of NGC 5548 and a nearby comparison star simultaneously, and calibrate the spectra of the object by using the comparison star. This procedure gives a calibration accuracy of  $\sim 2\%$  for NGC 5548 (see more details in Lu et al. 2016); (2) The instrument broadening is  $\sim 500$  km s $^{-1}$  (see Du et al. 2016), which is much less than the FWHM of the H $\beta$  line in the mean spectrum ( $\sim 9912 \pm 362$  km s $^{-1}$ , see Table 4 in Lu et al. 2016); (3) The time span of this observation is 205 days (with 61 epochs); (4) We used a spectral fitting scheme to measure the continuum and H $\beta$  line fluxes (see details in Hu et al. 2015; Lu et al. 2016), which allows us to remove the irrelevant spectral components as the He II and Fe II emission, the narrow lines, and the host galaxy. In the MEM analysis of our observation, we use the broad H $\beta$  profiles after subtracting those irrelevant components.

## 3. MEM FITTING

MEM is an effective method for fitting data without assuming any algebraic form of the model. The method has been applied to the RM observations, and successfully recovered their corresponding velocity-delay maps of about 11 sources (see Ulrich & Horne 1996; Bentz et al. 2010b; Grier et al. 2013; Xiao et al. 2018). The principle and equations of the MEM have been described in Horne (1994) and Xiao et al. (2018), and we make a brief overview here. Generally speaking, MEM introduces a linearized echo model (Equation 1; for convenience, we discretize it)

$$L(v_i, t_k) = \bar{L}_0(v_i) + \sum_j \Psi(v_i, \tau_j) [C(t_k - \tau_j) - \bar{C}_0] \Delta\tau \quad (2)$$

to fit the observed continuum light curve and the variations of the emission-line profiles. The velocity-delay map  $\Psi(v_i, \tau_j)$ , the continuum  $C(t_k)$ , and the background spectrum  $\bar{L}_0(v_i)$  are treated as parameterized model in the MEM fitting. Here  $\bar{L}_0(v_i)$  is designed to account for the non-variable component of the emission line, and  $\bar{C}_0$  is a reference continuum level, where we adopt the median of the continuum flux as  $\bar{C}_0$ . The MEM fitting is accomplished by minimizing

$$Q = \chi^2 - \alpha S, \quad (3)$$

where  $\chi^2 = \sum_m [D_m - \mathcal{M}_m(\vec{p})]^2 / \sigma_m^2$  constrains the “goodness-of-fitting” by “pulling” the model  $\mathcal{M}_m(\vec{p})$  toward

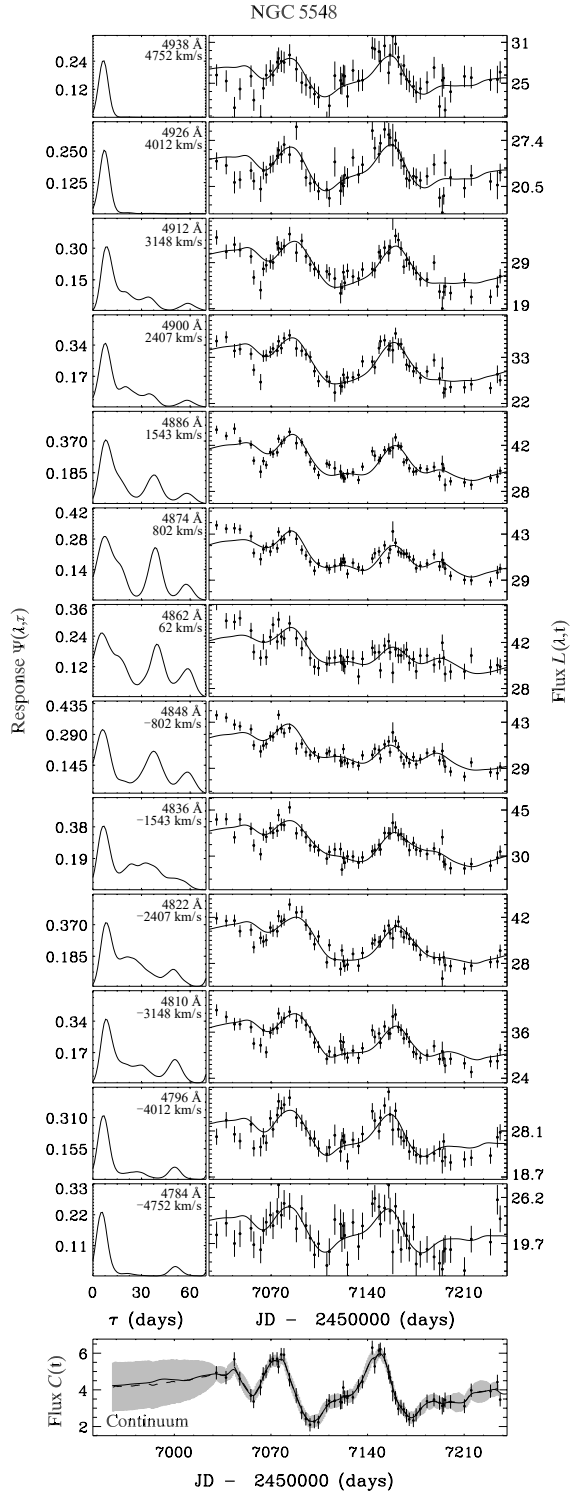


**Figure 1.** Some examples of the light curve fitting at different wavelengths (in the rest frame) for NGC 5548. The left panels show the corresponding 1-dimensional response functions. The bottom panel shows the original continuum light curve (black dots with error bars), the MEM reconstruction of the continuum (solid black line), and a damped random walk modeling (dashed line with gray envelope) for comparison. The selected wavelengths are labeled along the top axis of Figure 3.  $C(t)$  and  $L(\lambda, t)$  are in units of  $10^{-15} \text{ erg s}^{-1} \text{ cm}^{-2} \text{ \AA}^{-1}$  and  $10^{-16} \text{ erg s}^{-1} \text{ cm}^{-2} \text{ \AA}^{-1}$ , respectively.

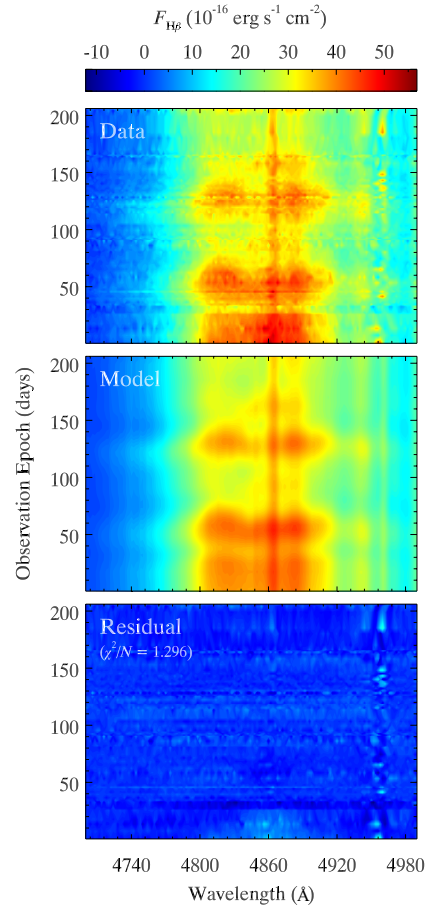


**Figure 2.** The observed time series of H $\beta$  emission line profiles, the overall MEM fits, and the residual.

the data  $D_m$  ( $D_m$  and  $\mathcal{M}_m(\vec{p})$  include the emission line and continuum light curves),  $S = \sum_n [p_n - q_n - p_n \ln(p_n/q_n)]$  is the entropy which controls the “simplicity-of-modeling” by minimizing the differences between the model parameters  $p_n$  and the “default image”  $q_n$ . Here  $m$  and  $n$  denote the numbers of the observational points and the parameters in the model, respectively. The parameter  $\alpha$  controls a trade-off between the “goodness-of-fitting” and the “simplicity-of-modeling”, which means increasing  $\alpha$  smooths the MEM model and leads to larger  $\chi^2/N$ , and vice versa. The model parameter  $p_n$  includes  $\Psi(v_i, \tau_k)$ ,  $C(t_k)$  and  $\bar{L}_0(v_i)$ , and  $q_n$  is designed as the geometric mean of  $p_n$ . For one-dimensional model components ( $C(t)$  and  $\bar{L}_0(v)$ ), we define

$$q(x) = \sqrt{p(x - \Delta x)p(x + \Delta x)}, \quad (4)$$

where  $x$  is  $t$  or  $v$  for  $C(t)$  or  $\bar{L}_0(v)$ , respectively, and for two-dimensional model ( $\Psi(v, \tau)$ ):

$$\ln q(v, \tau) = \frac{1}{1 + \mathcal{A}} \left[ \ln \sqrt{p(v - \Delta v, \tau)p(v + \Delta v, \tau)} + \mathcal{A} \ln \sqrt{p(v, \tau - \Delta \tau)p(v, \tau + \Delta \tau)} \right]. \quad (5)$$

Here  $\mathcal{A}$  is a parameter which assigns the weight and controls the aspect ratio of  $\Psi(v_i, \tau_k)$  in  $v$  and  $\tau$  direction. Increasing  $\mathcal{A}$  smears out the fine structures along the  $v$  direction, and vice versa. In this way, the total entropy can be written as  $S = (S_{\bar{L}_0} + \mathcal{W}_\Psi S_\Psi + \mathcal{W}_C S_C)/(1 + \mathcal{W}_\Psi + \mathcal{W}_C)$ , where  $\mathcal{W}_\Psi$  and  $\mathcal{W}_C$  are weight parameters which control the relative “stiffness” of  $L(v_i, t_k)$ ,  $C(t_k)$  and  $\bar{L}_0(v_i)$ . In the MEM fitting,  $\alpha$ ,  $\mathcal{A}$ ,  $\mathcal{W}_\Psi$  and  $\mathcal{W}_C$  are the user-controlled parameters. The selection of these parameters has been discussed in Xiao et al. (2018).

Similar to Grier et al. (2013) and Xiao et al. (2018), we first model the continuum by using the damped random walk (DRW, Li et al. 2013; Zu et al. 2013), then use the resulting highly sampled continuum in the MEM fitting instead of the original one. One benefit of this approach is that the DRW model can give reliable uncertainties. Additionally, the DRW model can be used to extrapolate the continuum light curve to times shortly before the campaign began, and thus provide better constraints on the MEM continuum modeling.

In Figure 1, we demonstrate the MEM fitting of the emission-line light curves at some uniformly-spaced (in velocity space) wavelengths, and draw the corresponding one-dimensional transfer functions in the left panels. The reconstruction of the continuum is shown in the bottom panel. It is obvious that the transfer functions of the line wings exhibit simple structures (basically show only one dominant peak), whereas the transfer functions around the line core are relatively complex with at least two peaks.

In order to better illustrate the overall fitting, we compare the time series of the line profiles and the corresponding MEM recovery in Figure 2. In general, the model fits nicely with the  $H\beta$  line profiles at all epochs, and the  $\chi^2/N$  of the overall fitting is 1.296. In addition, the residual (bottom panel of Figure 2) shows some weak signals (at  $\sim 4959 \text{ \AA}$  and  $\sim 4861 \text{ \AA}$ ), which are coming from the imperfect [O III]  $\lambda 4959$  and  $H\beta$  narrow line subtractions.

#### 4. THE VELOCITY-DELAY MAP

Figure 3 plots the  $H\beta$  velocity-delay map of NGC 5548 recovered from our data. We mark the wavelengths, which are selected to be shown in Figure 1, in its top axis. The map shows a symmetric “bell” shape, with a wide velocity distribution at short lags ( $\lesssim 15$  days) and a narrower velocity dispersion at longer lags. The broad wings extend to  $\sim \pm 7200 \text{ km s}^{-1}$ , while the response in the line core extends to  $\sim 48$  days. In addition, there is a hollow in the core of the map, and the response is relatively weaker at  $\sim [2400 \text{ km s}^{-1}, 28 \text{ days}]$ . For comparison, we plot the “virial envelope”  $v^2 = GM_\bullet/c\tau$  in Figure 3 with dotted lines, where  $M_\bullet$  is the black hole mass,  $G$  is the gravitational constant, and  $c$  is the speed of light. Here we adopt  $M_\bullet = 8.71 \times 10^7 M_\odot$  in Lu et al. (2016). The line re-

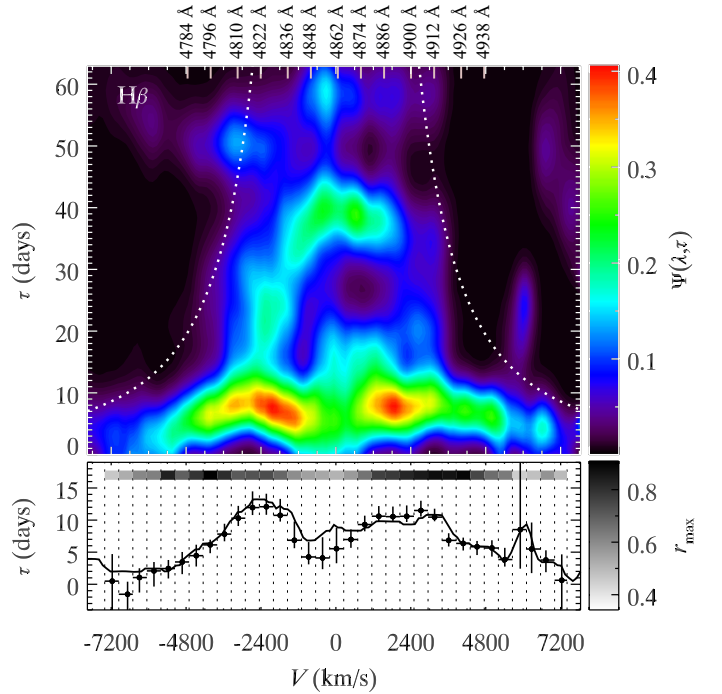


**Figure 3.** Top panel:  $H\beta$  velocity-delay map of NGC 5548. The dotted lines show the “virial envelope”  $V^2\tau c/G = 8.71 \times 10^7 M_\odot$ , based on the “virial product” measured from the mean time lag and the line dispersion (Lu et al. 2016). The labels on the top axis are the corresponding wavelengths selected in Figure 1. Bottom panel: The centroid time lag of the velocity-delay map (solid line), the velocity-resolved measurements (black dots), and the corresponding maximum cross-correlation coefficients  $r_{\max}$  (gray-scale bars).

sponse is compatible with the envelope, despite the weak “spine” at  $[v \sim 6000 \text{ km s}^{-1}, \tau \sim 12 - 30 \text{ days}]$  and the “blob” close to the line core at  $\sim 60$  days which are affected by the residuals coming from [O III]  $\lambda 4959$  and  $H\beta$  narrow line subtractions, respectively. There is a weak response at  $\sim [-3000 \text{ km s}^{-1}, 50 \text{ days}]$ , by comparing with the error map in Figure 5 (see the next section), this weak feature is significant. Its origin and evolution merit further investigations.

In Figure 3, we also demonstrate a comparison between the mean time lags at different velocities in our map and the velocity-resolved time-lag measurements. Here the velocity-resolved time lags are derived by dividing the  $H\beta$  profile into 33 uniformly-spaced ( $450 \text{ km s}^{-1}$ ) bins, and cross-correlating the  $H\beta$  light curve in each bin with the continuum (see more details in Lu et al. 2016). This result is essentially identical to that presented in Lu et al. (2016), although the  $H\beta$  profile is divided into narrower bins. The corresponding maximum cross-correlation coefficients ( $r_{\max}$ ) are marked by the gray-scale bars. To do the comparison, we convolve the velocity-delay map with the autocorrelation function (ACF) of the continuum (the output is identical to the CCF), and calculate the centroid around the peaks

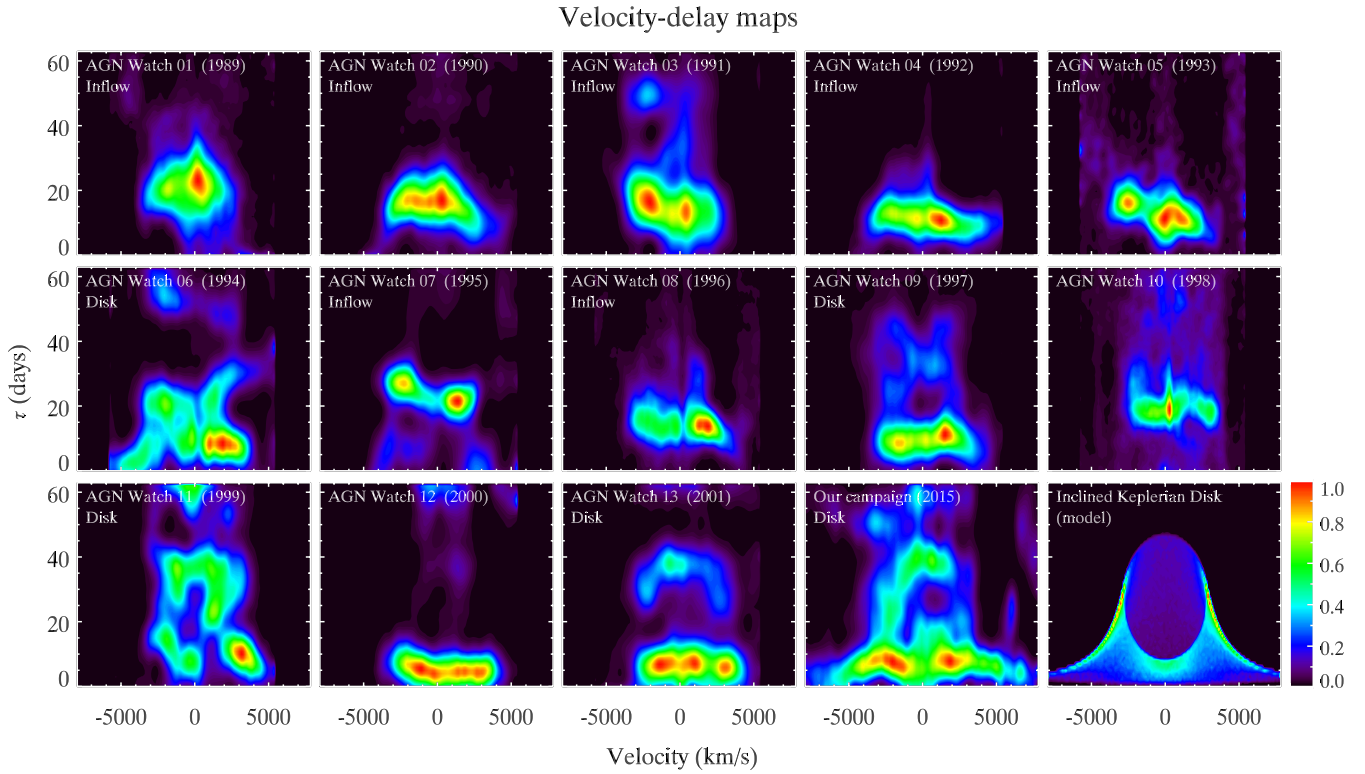


**Figure 4.**  $H\beta$  velocity-delay maps recovered from the AGN Watch data (first 13 panels), the  $H\beta$  map of our campaign (penultimate panel), and the simulated map of an inclined Keplerian disk (last panel). We normalize the maps and make their peak values equal to 1.

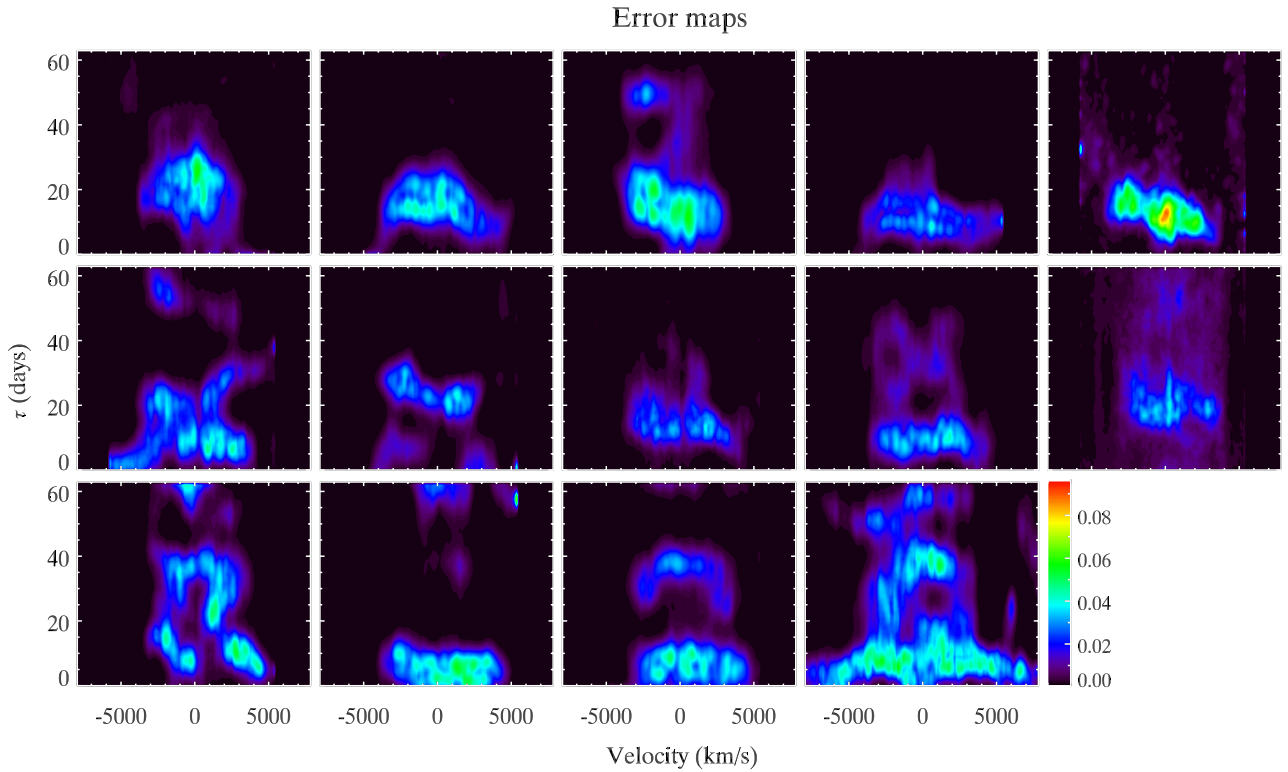


**Figure 5.** The standard deviations of the velocity-delay maps shown in Figure 4. We normalize the panels by the same factors of Figure 4.

(> 80%) of the outputs as the mean time lags. As expected, in general, the two results are consistent. The double-peaked structure of the velocity-resolved lags is similar to what was found by Pei et al. (2017) for the 2014 campaign.

Theoretically, a virialized BLR produces a velocity-symmetric signature like “bell” shape. This is because the velocity-delay structure of a Keplerian orbit is an ellipse, the orbits at inner (outer) radii of a virialized BLR produce ellipse structures on the map with wider (narrower) velocity distribution at shorter (longer) time delay, and the map is confined within the “virial envelope” (e.g., Bentz et al. 2010b; Grier et al. 2013; Xiao et al. 2018). In particular, the map of an inclined Keplerian disk has a lack of response in the core, and is different from the signature of a spherical shell, which has a filled ‘bell’ shape (e.g., see Figure 1 of Horne et al. 2004 and Figure 14 of Grier et al. 2013).

The “bell-like” velocity-delay map of NGC 5548 implies that its BLR is probably an inclined disk. It is unlikely to explain the map as a spherical shell geometry, because of the response deficit from  $\sim 20$  days to  $\sim 32$  days. The response of the map on the red side at  $\sim [2400 \text{ km s}^{-1}, 28 \text{ days}]$  is relatively weaker. Considering that the response of this area comes from the outer part of the BLR, such evidence indicates that the  $H\beta$  response at the outer radius may be more anisotropic or inhomogeneous.

## 5. LONG-TERM VARIABILITY

In order to investigate the long-term variability of the BLR kinematics and geometry, we compile the historical spectroscopic data from the AGN Watch archive<sup>1</sup>, which is by far the largest optical monitoring project of NGC 5548. This project involves 13 observing campaigns from Dec 1988 to Sept 2001, and each campaign has a time span of more than  $\sim 280$  days. The spectra are calibrated by using the [O III] narrow emission line as in Peterson et al. (2002). We did not apply the fitting scheme described in Section 2 to the AGN Watch data.

In Figure 4, we present the 13 velocity-delay maps recovered from the AGN Watch data together with our map (the same as in Figure 3). For comparison, we draw a simulated velocity-delay map for an inclined Keplerian disk in the bottom right panel of Figure 4. The disk is inclined ( $i = 45^\circ$  to the observer) with an inner radius of  $R_{\text{in}} = 3 \text{ lt-days}$  and an outer radius of  $R_{\text{out}} = 28 \text{ lt-days}$ , the emissivity distribution of the BLR clouds is assumed to be  $\epsilon \propto R^{-1}$ . The AGN Watch maps are denoted as AGN Watch 01-13. We apply the flux randomization (see details in Peterson et al. 1998), which modify the flux of each datum by a random Gaussian deviate within the flux uncertainty, and use the Monte Carlo (MC) simulations to calculate the uncertainties of the

velocity-delay maps. The error maps are shown in Figure 5. Given the error maps, the differences between the velocity-delay maps are significant. From the AGN Watch 01 to 05, the maps show continuing inflow signatures with longer lags at the blue end and shorter lags toward the red end. Interestingly, at this period, the average time lags are generally decreasing as well (see Table 8 in Peterson et al. 2002). The AGN Watch 07 to 08 are also dominated by inflow signatures with a decrease in the time lags. It implies that the shrink of its BLR may correlate to the inflow dynamics. It has been illustrated that the BLR size of NGC 5548 follows its continuum luminosity (Kilerci Eser et al. 2015). However, subsequent study reveals that the variation of the BLR size lags  $2.35^{+3.47}_{-1.25}$  yrs behind the luminosity change, and this lag is similar to the dynamical timescale ( $\sim 2.1$  yrs) of its BLR (Lu et al. 2016). The recombination timescale is insufficient to explain the variation of the BLR time lag, the change of its BLR kinematics is needed (Lu et al. 2016). The maps of the AGN Watch 06, 09, 11, and 13 generally show symmetric signatures with a paucity of response in the cores, which are similar to the signature of an inclined disk found in our map. They reveal that the BLR is disk-dominated in these periods. However, the detections of the response are limited by the data quality. The rest of the maps are not well recovered due to the low sampling rate or the small  $H\beta$  variability (see Table 6 and 7 in Peterson et al. 2002). Figure 4 shows a chronological series of the velocity-delay maps, indicating transitions between inflows and virialized status. This provides evidence for the BLR origin from the tidally disrupted clumps from the torus (Wang et al. 2017).

## 6. SUMMARY

We present the high-quality  $H\beta$  velocity-delay map of NGC 5548 recovered from our RM campaign in 2015. The map clearly shows a symmetric “bell-like” signature with a lack of response in the core. Such a structure is in accord with the predicted map of a Keplerian disk. The weaker response in the red than in the blue side at  $\sim 28$  days of the map indicates that the response at the outer radius of the BLR may be anisotropic or inhomogeneous. We also show the velocity-delay maps constructed from the 13-years AGN Watch data. The maps of the seven years reveal that the decreasing BLR size is probably related to the inflowing BLR gas. The other four maps show potential disk signatures which are consistent with our map. The velocity-delay maps of NGC 5548 imply that its BLR was switching between the inflow and virialized status in the past years.

We thank the anonymous referee for constructive suggestions. We thank Hong-Tao Liu for the supports of providing the computing resources, and Michael S. Brotherton for his helpful suggestions that improved the manuscript. We

<sup>1</sup> <http://www.astronomy.ohio-state.edu/~agnwatch/>

acknowledge the support of the staff of the Lijiang 2.4m telescope. Funding for the telescope has been provided by CAS and the People's Government of Yunnan Province. This research is supported by the National Key R&D Program of China (grants 2016YFA0400701 and 2016YFA0400702),

by NSFC through grants NSFC-11503026, -11233003, -11573026, -11703077, -11773029, by Grant No. QYZDJ-SSWSLH007 from the Key Research Program of Frontier Sciences, CAS, and by the Key Research Program of the CAS (grant No. KJZD-EW-M06). This work has made use of data from the AGN Watch archive.

## REFERENCES

- Bahcall, J. N., Kozlovsky, B.-Z., & Salpeter, E. E. 1972, *ApJ*, 171, 467
- Barth, A. J., Nguyen, M. L., Malkan, M. A., et al. 2011, *ApJ*, 732, 121
- Barth, A. J., Pancoast, A., Thorman, S. J., et al. 2011, *ApJL*, 743, L4
- Bentz, M. C., Denney, K. D., Cackett, E. M., et al. 2007, *ApJ*, 662, 205
- Bentz, M. C., Walsh, J. L., Barth, A. J., et al. 2008, *ApJL*, 689, L21
- Bentz, M. C., Walsh, J. L., Barth, A. J., et al. 2009, *ApJ*, 705, 199
- Bentz, M. C., Walsh, J. L., Barth, A. J., et al. 2010, *ApJ*, 716, 993
- Bentz, M. C., Horne, K., Barth, A. J., et al. 2010, *ApJL*, 720, L46
- Blandford, R. D., & McKee, C. F. 1982, *ApJ*, 255, 419
- Edelson, R., Gelbord, J. M., Horne, K., et al. 2015, *ApJ*, 806, 129
- De Rosa, G., Peterson, B. M., Ely, J., et al. 2015, *ApJ*, 806, 128
- Denney, K. D., Watson, L. C., Peterson, B. M., et al. 2009, *ApJ*, 702, 1353
- Denney, K. D., Peterson, B. M., Pogge, R. W., et al. 2009, *ApJL*, 704, L80
- Denney, K. D., Peterson, B. M., Pogge, R. W., et al. 2010, *ApJ*, 721, 715
- Doroshenko, V. T., Sergeev, S. G., Klimanov, S. A., Pronik, V. I., & Efimov, Y. S. 2012, *MNRAS*, 426, 416
- Du, P., Lu, K.-X., Hu, C., et al. 2016, *ApJ*, 820, 27D
- Du, P., Zhang, Z.-X., Wang, K., et al. 2018, *ApJ*, 856, 6
- Fausnaugh, M. M., Denney, K. D., Barth, A. J., et al. 2016, *ApJ*, 821, 56
- Grier, C. J., Peterson, B. M., Pogge, R. W., et al. 2012, *ApJ*, 755, 60
- Grier, C. J., Peterson, B. M., Horne, K., et al. 2013, *ApJ*, 764, 47
- Grier, C. J., Pancoast, A., Barth, A. J., et al. 2017, *ApJ*, 849, 146
- Horne, K., Welsh, W. F., & Peterson, B.M. 1991, *ApJL*, 367, 5
- Horne, K. 1994, in *ASP Conf. Ser. 69, Reverberation Mapping of the Broad-line Region in Active Galactic Nuclei*, ed. P.M. Gondhalekar, K. Horne, & B.M. Peterson (San Francisco, CA: ASP), 23
- Horne, K., Peterson, B. M., Collier, S. J., & Netzer, H. 2004, *PASP*, 116, 465
- Hu, C., Du, P., Lu, K.-X., et al. 2015, *ApJ*, 804, 138
- Kaspi, S., Smith, P. S., Netzer, H., et al. 2000, *ApJ*, 533, 631
- Kilerci Eser, E., Vestergaard, M., Peterson, B. M., Denney, K. D., & Bentz, M. C. 2015, *ApJ*, 801, 8
- Kollatschny, W., & Zetzl, M. 2013, *A&A*, 551, L6
- Krolik, J. H., & Done, C. 1995, *ApJ*, 440, 166
- Li, Y.-R., Wang, J.-M., Ho, L. C., Du, P., & Bai, J.-M. 2013, *ApJ*, 779, 110
- Lu, K.-X., Du, P., Hu, C., et al. 2016, *ApJ*, 827, 118
- Murray, N., & Chiang, J. 1997, *ApJ*, 474, 91
- Pancoast, A., Brewer, B. J., & Treu, T. 2011, *ApJ*, 730, 139
- Pancoast, A., Brewer, B.J., Treu, T., et al. 2012, *ApJ*, 730, 139
- Pancoast, A., Brewer, B.J., & Treu, T. 2014, *MNRAS*, 445, 3055
- Pancoast, A., Brewer, B.J., & Treu, T. 2014, *MNRAS*, 445, 3073
- Pancoast, A., Barth, A. J., Horne, K., et al. 2018, *ApJ*, 856, 108
- Pei, L., Fausnaugh, M. M., Barth, A. J., et al. 2017, *ApJ*, 837, 131
- Peterson, B. M., Ali, B., Horne, K., et al. 1993, *PASP*, 105, 247
- Peterson, B. M., Wanders, I., Horne, K., et al. 1998, *PASP*, 110, 660
- Peterson, B. M., Berlind, P., Bertram, R., et al. 2002, *ApJ*, 581, 197
- Peterson, B. M., Ferrarese, L., Gilbert, K. M., et al. 2004, *ApJ*, 613, 682
- Proga, D., & Kallman, T. R. 2004, *ApJ*, 616, 688
- Skjelboe, A., Pancoast, A., Treu, T., et al. 2015, *MNRAS*, 454, 144
- Ulrich, M.-H., & Horne, K. 1996, *MNRAS*, 283, 748
- Wang, J.-M., Du, P., Brotherton, M. S., et al. 2017, *Nature Astronomy*, 1, 775
- Xiao, M., Du, P., Horne, K. D., et al. 2018, *arXiv:1808.00705*
- Zu, Y., Kochanek, C. S., Kozlowski, S., & Udalski, A. 2013, *ApJ*, 765, 106